

Chip-scale high-peak-power semiconductor/solid-state vertically integrated laser

Received: 2 April 2022

Accepted: 22 September 2022

Published online: 01 October 2022

 Check for updates

Jianglin Yue¹, Kenji Tanaka¹, Go Hirano¹, Gen Yonezawa¹, Misaki Shimizu¹, Yasunobu Iwakoshi¹, Hiroshi Tobita¹, Rintaro Koda², Yasutaka Higa², Hideki Watanabe², Katsunori Yanashima¹ & Masanao Kamata¹ ✉

Compact lasers capable of producing kilowatt class peak power are highly desirable for applications in various fields, including laser remote sensing, laser micromachining, and biomedical photonics. In this paper, we propose a high-peak-power chip-scale semiconductor/solid-state vertically integrated laser in which two cavities are optically coupled at the solid-state laser gain medium. The first cavity is for the intra-pumping of ytterbium-doped yttrium aluminum garnet (Yb:YAG) with an electrically driven indium gallium arsenide (InGaAs) quantum well, and the second cavity consists of Yb:YAG and chromium-doped yttrium aluminum garnet (Cr:YAG) for passive Q-switching. The proposed laser produces pulses as short as 450 ps, and an estimated peak power of 57.0 kW with a laser chip dimension of 1 mm³. To the best of our knowledge, this is the first monolithic integration of semiconductor and solid-state laser gain mediums to realize a compact high-peak-power laser.

High-peak-power solid-state lasers have played an important role in modern science and technology, with widespread applications in various fields, including laser remote sensing^{1,2}, laser micromachining^{3,4}, and biomedical photonics^{5,6}. In line with the progress of semiconductor lasers as pumping sources, the past three decades have seen the emergence of various types of high-peak-power solid-state lasers. These lasers can be classified into categories: laser cavity configurations (fiber lasers⁷, thin-disk lasers⁸, slab lasers⁹, and microchip lasers^{10,11}, starting from the original rod geometry^{12,13}), pulsation methods¹⁴ (Q-switching, cavity-dumping, and mode-locking), etc. Among the pulsation techniques, Q-switching is one of the most successful approaches to obtain kilowatt class laser peak power for science and industry with relative ease, in which a much larger population inversion can be attained by removing cavity feedback to a point, where a sudden change of the cavity Q factor causes the generation of short intense laser pulses. Given that the fluorescent lifetimes of solid-state laser mediums are on the order of microsecond to millisecond¹⁵, which are several magnitudes of orders larger than that of semiconductor gain mediums^{16,17}, they are suitable for producing short-pulse high-peak-power laser with excellent beam quality. However, unlike semiconductor lasers, which can be electrically driven, the solid-

state laser mediums comprise dielectrics or glasses and require an external laser for pumping, thereby making compact chip-scale high-peak-power lasers very challenging. Therefore, their potential applications are hampered via the system size and assembling cost. Thus, to reach the same maturity level as existing semiconductor lasers, which are suitable for miniaturization and cost-effective mass production, the integration of all elements monolithically compatible with wafer-level manufacturing is required. Meanwhile, as an approach from semiconductor lasers, 2D photonic crystal surface-emitting lasers have recently attracted much attention due to their capability of large-area 2D coherent lasing oscillation of several millimeters, which is much larger than that of conventional semiconductor lasers. A peak power of 18 W has been reported experimentally and up to 300 W can be expected via optimization¹⁸. Here, we introduce another option for high-peak-power operation exceeding kilowatt, which has not been demonstrated yet for fully integrated chip-scale lasers.

In this work, we originally demonstrate to the best of our knowledge, a fully integrated chip-scale, compact, passively Q-switched laser comprising a semiconductor laser medium and a solid-state laser medium with a peak power, pulse width, and volume of 57.0 kW, 450 ps, and 1 mm³, respectively.

¹Tokyo Laboratory 04, R&D Center, Sony Group Corporation, Atsugi, Kanagawa 243-0014, Japan. ²Tokyo Laboratory 06, R&D Center, Sony Group Corporation, Atsugi, Kanagawa 243-0014, Japan. ✉ e-mail: masa.kamata@sony.com

Results

Concept

To integrate a semiconductor laser and solid-state laser monolithically, a vertical-cavity surface-emitting laser (VCSEL) is more attractive compared to an edge-emitting laser as a pumping laser source because it can emit a laser beam perpendicular to its surface, making it suitable for vertical integration. However, as the volume of the active region of the single-emitter VCSEL is small, the laser output is substantially limited. Therefore, the following problems occur when a solid-state laser is externally pumped. First, it is necessary to use an optical lens to focus the pumping laser beam, which complicates the system configuration and makes vertical integration difficult. Second, as the pumping laser passes through the solid-state laser medium only once or at most twice, the thickness of the solid-state laser medium should be of the same order as the absorption length, which is undesirable from the viewpoint of manufacturing via vertical integration.

To solve these problems, we employ a vertical-external-cavity surface-emitting laser (VECSEL) as an intra-cavity pumping source. Figure 1 illustrates a schematic of our proposed chip-scale semiconductor/solid-state vertically integrated laser, in which two cavities are optically coupled at the solid-state laser gain medium. The first cavity is a VECSEL for intra-pumping of Yb:YAG, with an electrically driven InGaAs quantum well, and the second cavity is for passive Q-switching that comprises Yb:YAG and Cr:YAG. This configuration provides the following advantages. First, as the pumping laser beam is focused via the thermal lens generated at the GaAs substrate and Yb:YAG, the optical lens necessary for external pumping configuration is not required. Second, via intra-pumping, even when the single-pass absorption rate of the Yb:YAG is low, the pumping laser can be efficiently absorbed and the thickness of the Yb:YAG can be reduced. Thus, vertical integration is possible in the proposed configuration.

The VECSEL cavity based on InGaAs quantum well ($\lambda = 940$ nm) comprises two highly reflective (HR) layers at both ends and an intermediate partially reflective (PR) layer. An HR layer is a p-type distributed Bragg reflector (p-DBR), and the other is a dielectric coating layer between the Yb:YAG and Cr:YAG. The intermediate PR layer is an n-type DBR (n-DBR). The VECSEL cavity has no output coupling other than the absorption in the Yb:YAG. The passively Q-switched laser cavity ($\lambda = 1030$ nm) comprises two reflective layers at both ends, where one is an HR layer and the other is a PR layer that acts as an output coupler (OC) for laser emission. The Yb:YAG is selected as a

solid-state gain medium, in which high quantum efficiency is expected in the combination of 940 nm pumping and 1030 nm Q-switched laser oscillation. By injecting current into the InGaAs quantum well, which is inside the VECSEL cavity, the 940 nm pumping laser and 1030 nm passively Q-switched laser oscillate successively, thereby causing the emission of a short pulse with high-peak-power.

VECSEL cavity design

To achieve Q-switched oscillation in the proposed laser configuration, we first design the configuration of the VECSEL cavity. Although there are several advantages with intra-cavity pumping as mentioned above, it has an inherent trade-off. First, since the Yb:YAG is placed in the VECSEL cavity, its absorption for the gain of Q-switched oscillation becomes a loss factor for the pumping laser. Single-emitter VCSEL/VECSEL is quite sensitive to cavity loss due to the small gain; therefore, the introduction of the loss factor should be treated with careful attention. Second, the Yb:YAG obtains the gain of Q-switched oscillation at 1030 nm by absorbing the pumping laser at 940 nm; hence, it is desirable to increase its absorption as much as possible. This balance between the loss of the pumping laser and the gain of the Q-switched laser is one of the important design issues in the proposed laser configuration.

This trade-off can be understood in terms of characteristics of the external cavity part of the VECSEL cavity (Fig. 2a). There are four parameters in the external cavity part: reflectance of the n-DBR (R_2), reflectance of the HR layer at 940 nm (R_3), absorption rate of the GaAs substrate (A_{GaAs}), and absorption rate of the Yb:YAG (A_{Yb}). Because R_3 should be as high as 100% for effective intra-cavity pumping and A_{GaAs} is specific to the substrate condition, the parameters to be designed are R_2 and A_{Yb} . However, fully theoretical or numerical analysis of these two parameters is challenging because the dynamic change of the transverse mode at 940 nm must be included due to the thermal lens produced at the GaAs substrate and Yb:YAG, whose simulation is not easy to perform accurately. Instead, to obtain a design guideline for the VECSEL cavity, we develop a semiempirical model that combines experimental data and external cavity theory.

We first discuss the n-DBR reflectance R_2 . For efficient power build-up of the 940 nm laser in the cavity, R_2 should be as high as possible to overcome the loss factor in the external cavity part. However, an excessively high R_2 incurs a risk of VCSEL oscillations between the p-DBR and n-DBR (rather than VECSEL oscillations). In this oscillation mode, the pumping of the Yb:YAG is not intra-cavity pumping but external pumping, which prevents the effective pumping-power absorption of the Yb:YAG. Figure 2b shows the measured VECSEL output power for two semiconductor devices with $R_2 = 90.0\%$ and 96.1% . Note that a Yb:YAG was not inserted, and an external OC at 940 nm (reflectance: R_{940}) was placed for the VECSEL output oscillation. Between the two n-DBR conditions, a higher output power is obtained with $R_2 = 96.1\%$ as expected. It can also be seen that the output power varies with R_{940} . This variation comes from the change in effective reflectivity of the external cavity part (R_{eff}) due to R_{940} , indicating the proper occurrence of VECSEL oscillations.

We next discuss the Yb:YAG absorption rate A_{Yb} from the viewpoint of the pumping-power absorption of the Yb:YAG (P_{Yb}). As explained above, A_{Yb} is directly related to the trade-off between loss of the pumping laser and gain of the Q-switched laser. Figure 2c illustrates the relationship between A_{Yb} and P_{Yb} for $R_2 = 96.1\%$, which was analyzed using the measured output power (Fig. 2b) and the derived equations in the external cavity part (see Methods for details). When $A_{\text{Yb}} < 30\%$, P_{Yb} increases with increasing A_{Yb} , indicating that a higher Yb:YAG gain is expected at higher A_{Yb} . In contrast, when $A_{\text{Yb}} > 30\%$, the P_{Yb} decreases with increasing A_{Yb} because R_{eff} becomes smaller with higher A_{Yb} ; consequently, the condition shifts from the optimum R_{eff} condition.

To confirm the basic gain characteristic of our laser configuration at 1030 nm, a fundamental experiment of 1030 nm continuous wave

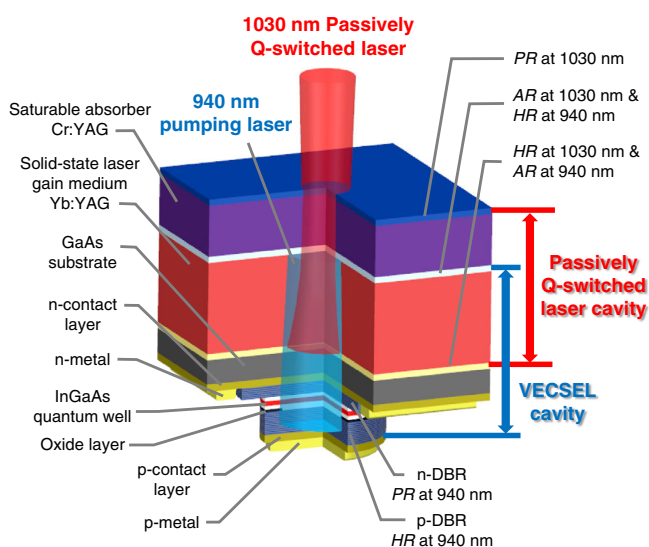


Fig. 1 | Schematic of chip-scale semiconductor/solid-state vertically integrated laser. The VECSEL cavity and the passively Q-switched laser cavity are optically coupled at the solid-state gain medium of Yb:YAG.

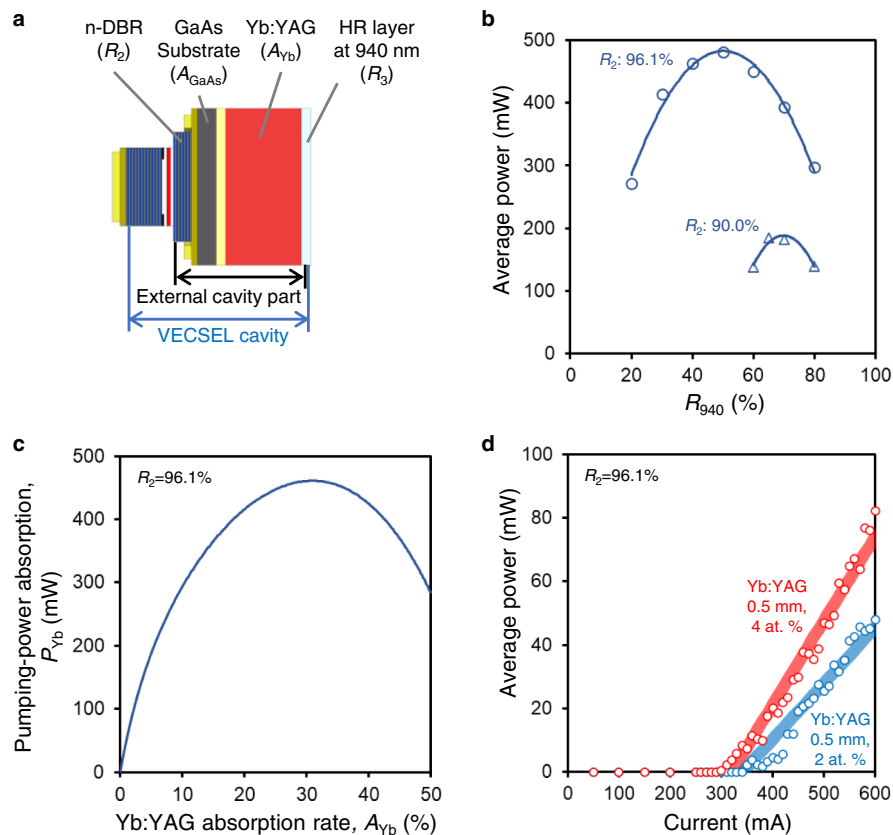


Fig. 2 | Design of the integrated VECSEL cavity. a VECSEL cavity model.

b Measured VECSEL output power for $R_2 = 90.0\%$ and 96.1% . The Yb:YAG was replaced by a 940 nm OC (reflectance: R_{940}). The distance between the GaAs substrate and OC was 0.5 mm. **c** Analyzed pumping-power absorption of Yb:YAG (P_{Yb}) versus Yb:YAG absorption rate (A_{Yb}) for $R_2 = 96.1\%$. Other parameters were set as

follows: $R_3 = 99.0\%$ and $A_{GaAs} = 7.0\%$. **d** Measured I-L characteristics in the 1030 nm CW laser oscillation experiment with a 1030 nm OC ($R_{oc} = 85\%$). The Yb:YAG was 0.5 mm thick and its doping concentration was 2 at. % ($A_{Yb} = 9.5\%$) or 4 at. % ($A_{Yb} = 18.1\%$).

(CW) oscillation was performed, in which a 1030 nm laser cavity only included a Yb:YAG (i.e., no saturable absorber). The detailed conditions were as follows: the thickness of the Yb:YAG was 0.5 mm, and the doping concentrations were 2 and 4 at. %, which corresponded to A_{Yb} of 9.5% and 18.1%, respectively. Both surfaces of the Yb:YAG were coated to form the VECSEL and 1030 nm cavities (see Methods for details of the Yb:YAG coating). An OC with a reflectance (R_{oc}) of 85% at 1030 nm was placed additionally. The semiconductor element was cooled to 20 °C by an active cooling system. Because of the difficulty of mechanical assembly, the Yb:YAG was placed at a distance of 0.4 mm from the semiconductor element. Figure 2d shows the current–output (I–L) characteristics of 1030 nm CW oscillation. A laser oscillation was confirmed at both doping concentrations. Moreover, a higher output power was achieved at 4 at. % ($A_{Yb} = 18.1\%$). This result agrees well with the analyzed pumping-power absorption in Fig. 2c, in which A_{Yb} of 18.1% realizes higher pumping-power absorption than A_{Yb} of 9.5%.

The development of the semiempirical model led to a method for deriving the VECSEL cavity parameters, especially the two important parameters R_2 and A_{Yb} .

Passively Q-switched laser simulation

To derive the passively Q-switched laser cavity configuration, we developed a simultaneous rate equations model between the VECSEL cavity and passively Q-switched laser cavity. This model can help us understand the carrier and photon dynamics of both the VECSEL and passively Q-switched cavities, which are driven electrically and optically, respectively. More details on this model can be found in the “Methods” section. Figure 3 illustrates the simulation results of the model. The configuration of the passively Q-switched laser simulation

consists of 0.5 mm thick Yb:YAG with a doping concentration of 4 at. %, 0.2 mm thick Cr:YAG with initial transmittance of 95%, and the OC with a reflectance of 85%.

The top part of Fig. 3a shows that when current is injected into the InGaAs quantum well of the VECSEL at an initial time ($t = 0 \mu\text{s}$), the carrier density (N) and photon density (S) increase and the oscillation of 940 nm pumping laser begins within a few nanoseconds. Then, the 940 nm pumping laser maintains a stable oscillation state ($t = 0\text{--}900 \mu\text{s}$). The bottom part of Fig. 3a shows that the population inversion density (N_g) increases when the 940 nm pumping laser is partially absorbed by the Yb:YAG, which means that energy is accumulated in the 1030 nm cavity for several hundred microseconds ($t = 0\text{--}470 \mu\text{s}$). When Cr:YAG is bleached, the cavity Q factor switches to a high value in a short time. Furthermore, the population inversion density decreases rapidly, and a high-peak-power laser pulse is generated with a pulse width of several hundred picoseconds (around $t = 470 \mu\text{s}$), as shown in Fig. 3b. After Q-switched laser pulse oscillation, the saturable absorber becomes unbleached again, the cavity Q factor switches to a low value and energy is accumulated for the next Q-switched laser pulse oscillation ($t = 470\text{--}740 \mu\text{s}$), as shown in Fig. 3a. From the top part of Fig. 3a, it is also found that photon density at 940 nm decreases slightly when 1030 nm picosecond pulses are generated. This phenomenon occurs because the ground-state population density of Yb^{3+} ion and the absorption at 940 nm increase by Q-switched laser pulse oscillation, and the photon density at 940 nm decreases after laser pulse oscillation.

The simulation results show that in our proposed laser configuration, the 940 nm pumping laser maintains a stable oscillation state, and 1030 nm passively Q-switched laser oscillation is theoretically possible.

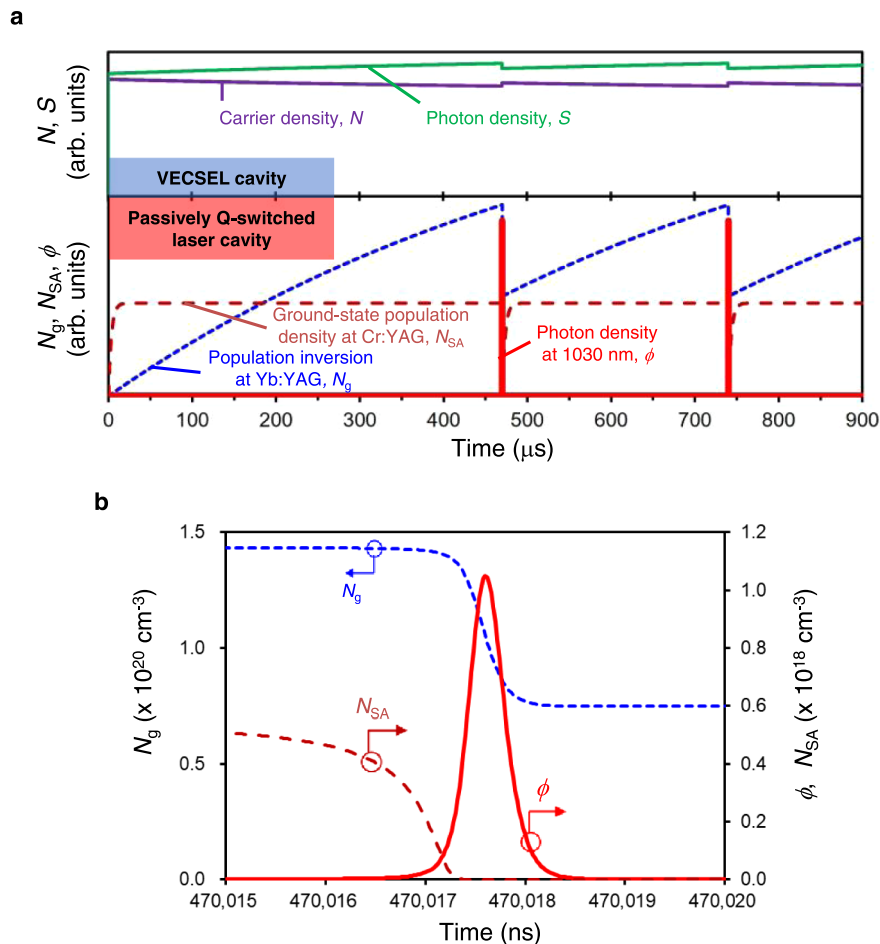


Fig. 3 | Simulation results of the simultaneous rate equations model. a (top) Temporal dynamics of the carrier and photon densities at 940 nm in the VECSEL cavity; (bottom) temporal dynamics of the population inversion density at Yb:YAG, ground-state population density at Cr:YAG, and photon density at 1030 nm in the

passively Q-switched laser cavity. **b** Temporal dynamics of the population inversion density in Yb:YAG, ground-state population density in Cr:YAG, and the photon density at 1030 nm at the time of Q-switching ($-470 \mu\text{s}$ in a).

Passively Q-switched laser demonstration

To demonstrate the concept of the proposed laser configuration, first, we fabricated a mechanically assembled semiconductor/solid-state vertically integrated laser for the ease of the experiment. Note that all elements were assembled mechanically, and there was a 0.4 mm air gap between the semiconductor element and the Yb:YAG due to the difficulty of the mechanical assembly as already mentioned. The laser device parameters and the cooling condition of the semiconductor element were the same as those described in the previous sections. Figure 4a shows the I–L characteristics, and a laser oscillation is confirmed at a current threshold value of 300 mA. Figure 4b, c show the single-pulse waveform and the temporal waveform, respectively, at an injection current of 370 mA. The temporal pulse profile was measured by a high-speed biased fiber-optic detector (Newport Corporation 818-BB-35F) with a bandwidth of 15 GHz and a digital phosphor oscilloscope (Tektronix TDS7404) with a bandwidth of 4 GHz (Sampling Rate: 20 GHz). The pulse width of 461 ps and the pulse trains (1.2 kHz repetition frequency) are confirmed, indicating that Q-switched oscillation has successfully occurred. The peak power (23.2 kW; see Fig. 4b) was estimated from its temporal pulse waveform with a pulse energy of 12.1 μJ measured by a pyroelectric energy meter (Ophir PE9-C). Figure 4d exhibits the laser spectrum measured under the same current condition. A single longitudinal mode with a peak wavelength at 1030.1 nm (measured by an optical spectrum analyzer with a resolution of 0.1 nm) is confirmed. These measured results demonstrate that

Q-switched oscillation is practically possible in our proposed laser configuration.

Next, we demonstrate Q-switched laser oscillation of a fully integrated 1 mm³ chip-scale laser. The cavity configuration of a fully integrated chip-scale laser differs from that of a mechanically assembled laser (See Methods for details of the device structure). Figure 5a shows the fabricated laser. All elements were successfully bonded together by chip-scale integration, and the laser was mounted on a transistor outline can (TO-can) with a diameter of 9 mm, which is commonly used in semiconductor laser packaging. Figure 5b shows the I–L characteristics after active cooling at 20 °C. A laser oscillation is confirmed at a current threshold of 280 mA. The following laser characteristics were measured under a current injection of 330 mA. The pulse energy remained stable for 2 h (Fig. 5c). The average pulse energy was 30.4 μJ with a standard deviation of 0.2 μJ and the repetition frequency was 1.79 kHz. Figure 5d shows the single-pulse waveform with a pulse width of 450 ps. The estimated peak power was as high as 57.0 kW. A single longitudinal mode at a wavelength of 1030.6 nm and M^2 of 1.36 (x axis) and 1.22 (y axis) are also confirmed (Fig. 5e, f). The output power was stable for 24 hours, and passively Q-switched oscillations with an average power of 53.5 mW and standard deviation of 0.3 mW were obtained (Fig. 5g) under the current injection of 330 mA, which is the same condition as the series of the laser characteristics measurements described above. Stability and lifetime tests for different driving currents are also planned for future studies. The series of experimental

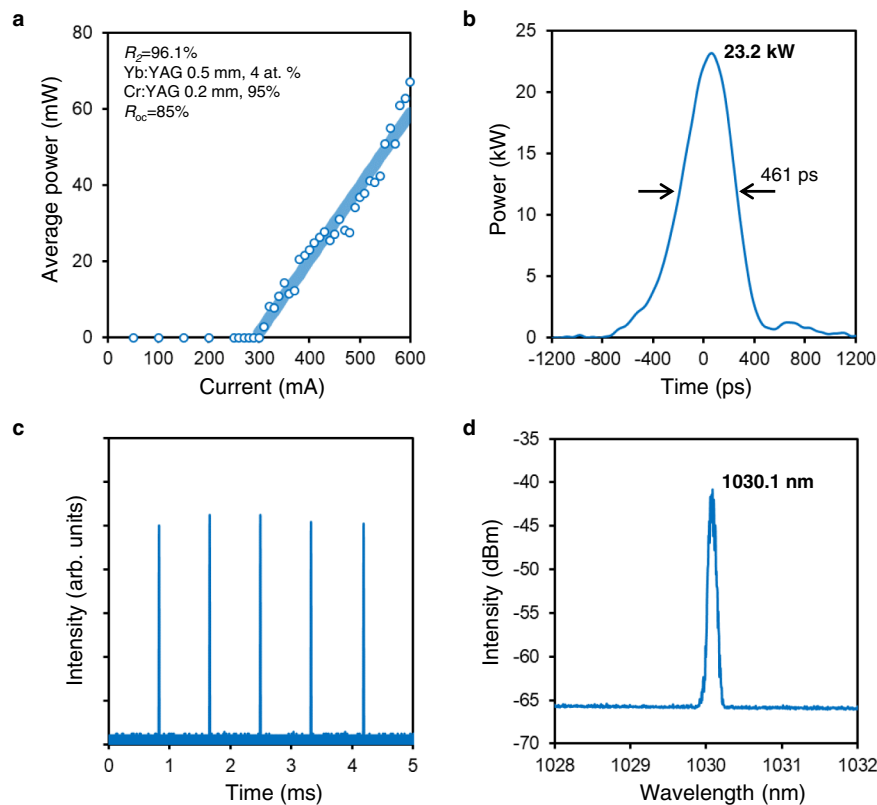


Fig. 4 | Experimental results of the mechanically assembled laser. **a** I–L characteristics. **b** Single-pulse waveform. The vertical axis was calculated from the obtained pulse energy (12.1 μ J) and the pulse waveform. **c** Temporal waveform.

d Optical spectrum. The data presented in **b–d** were measured at an injection current of 370 mA.

results demonstrate that our proposed laser configuration can realize a high-peak-power over kilowatts at the same chip-scale size as semiconductor lasers.

Some differences exist between the result of the mechanically assembled laser and that of the fully integrated chip-scale laser. In addition to the cavity configuration, these differences might arise from the VECSEL cavity length (air gap), the thermal diffusion effect between the semiconductor element and Yb:YAG, and individual differences among the elements (VECSEL, Yb:YAG, and Cr:YAG). Interaction among these factors should affect the coupled laser oscillation parameters such as pumping laser power, mode matching, absorption cross section, and stimulated emission cross-section of the Yb:YAG and Cr:YAG.

Discussion

The presented results provide clear evidence that the configuration of chip-scale high-peak-power lasers by vertical integration of semiconductor and solid-state laser gain mediums is possible, thereby bridging the gap between semiconductor lasers and solid-state lasers for the first time since their inventions. Although we chose the combination of InGaAs quantum well and Yb:YAG as gain mediums, other materials can easily be used to generate different laser wavelengths other than 1030 nm, so our approach opens a new door for establishing a versatile platform for compact high-peak-power lasers. By properly taking into consideration injection current distribution and mode matching between the VECSEL cavity and the passive Q-switched laser cavity, further power improvement should be possible by increasing the chip size. Moreover, as the laser is capable of wafer-level vertical integration, it can potentially be coupled with flat optics such as nanophotonic metasurfaces¹⁹ to customize its phase, amplitude, polarization, and beam direction.

This laser can be applied to several applications. Compact high-peak-power lasers are very promising in the field of light detection and

ranging (LiDAR) applications for autonomous driving cars, drones, and robots. The use of such lasers in LiDAR applications is necessary to meet the potential demands of a high-peak-power laser source on the size scale of semiconductor lasers, but no laser source currently meets this market demand.

Additionally, the proposed laser differs greatly from conventional solid-state lasers in terms of the ease of array arrangement. The minimum lateral size of our laser is determined via the oxide aperture diameter of the VECSEL, which is about 150 μ m. This means that many lasers can be arranged in parallel within one chip. Moreover, since the manufacturing process of the VECSEL uses a photolithography process, the array arrangement can be achieved with high positional accuracy (on the order of micrometers). This laser array device can benefit not only LiDAR, but also laser micromachining used in manufacturing and laser medical applications. In laser micromachining, irradiating a target area with a single laser beam causes significant thermal accumulation at a laser repetition rate of approximately 1 MHz²⁰. Therefore, the repetition rate cannot be simply raised to increase the throughput of laser micromachining. In such cases, parallel processing using arrayed laser beams is an effective alternative. Although a beam splitting device for this purpose has been reported²¹, it lacks flexibility because each arrayed laser beam cannot be switched independently since only one primary laser light source is used.

We believe that our lasers will transform the situation of conventional high-peak-power lasers, where potential effectiveness has been confirmed at the laboratory level, but actual field applications have been limited by cost and size constraints.

Methods

Device structure

Figure 1 illustrates a schematic of the proposed laser. The proposed laser consists of a VECSEL, solid-state laser gain medium, and saturable

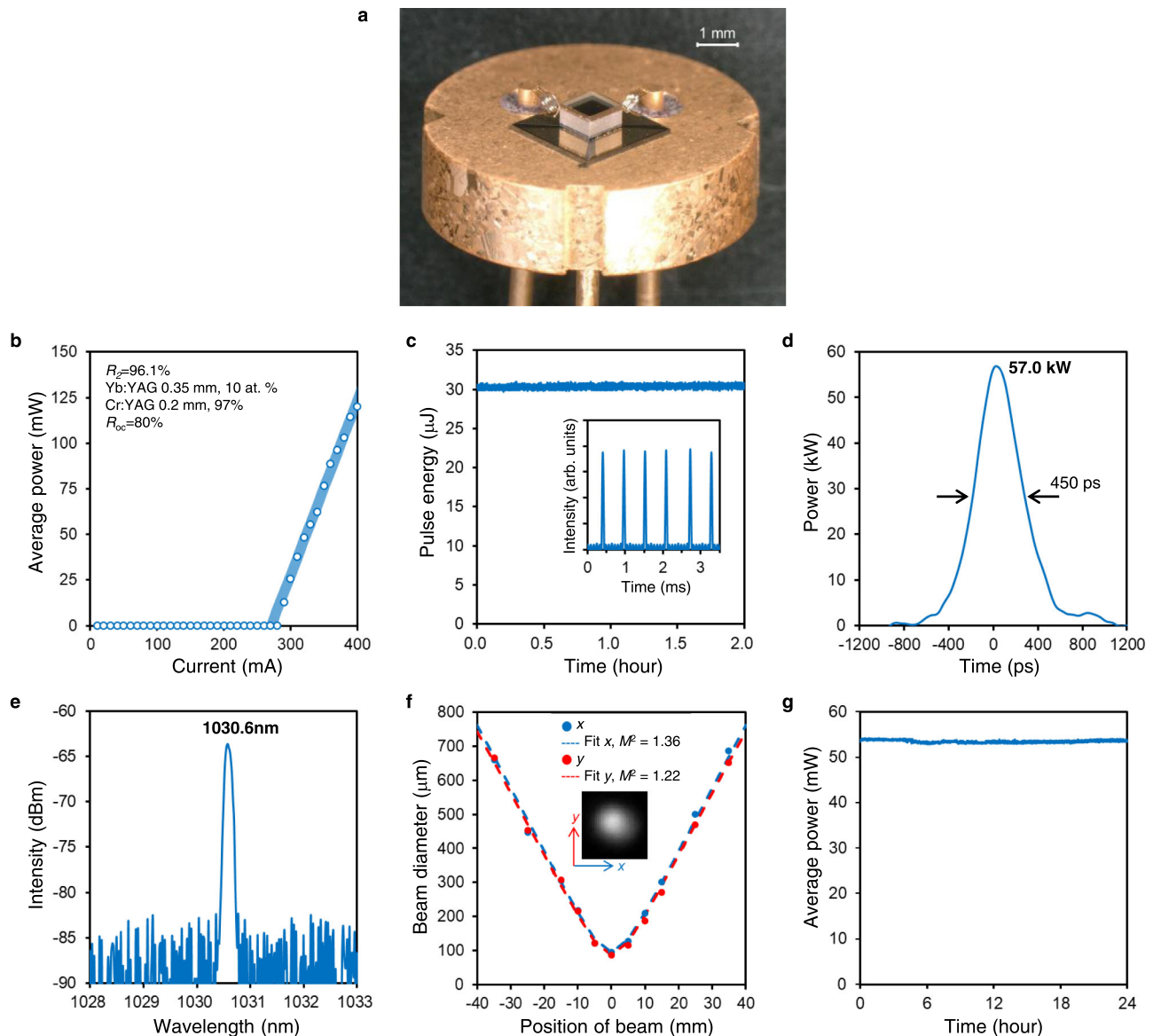


Fig. 5 | Demonstration of the chip-scale semiconductor/solid-state vertically integrated laser. **a** Photograph of the laser chip. **b** I–L characteristics. **c** Pulse energy stability (2 h) of the chip-scale integrated laser (inset: temporal waveform). **d** Single-pulse waveform. The vertical axis was calculated from the obtained pulse

energy (30.4 μJ) and the pulse waveform. **e** Optical spectrum. **f** M^2 (beam quality) measurements (inset: beam profile at the beam waist). **g** Output power stability for 24 hours. The data presented in **c–g** were measured at an injection current of 330 mA.

absorber, and each interface and emitting end has a dielectric multi-layer coating. Regarding the VECSEL, a p-DBR (GaAs/AlGaAs), an active layer (InGaAs quantum well), and an n-DBR (GaAs/AlGaAs) were grown on a GaAs substrate with p-/n-contact layers (GaAs) using metal–organic chemical vapor deposition. The reflectance of p-DBR and n-DBR were designed to be 99.9% and 96.1%, respectively. An oxide layer for current and optical confinement was located near the active layer with an aperture of 150 μm diameter created using a selective oxidation process. Electrodes were formed on p-/n-contact layers. To reduce the absorption loss at the wavelength of 940 nm, the GaAs substrate was thinned to 0.1 mm, whose surface was coated with an antireflection coating ($R < 1\%$ at 940 nm). For the mechanically assembled laser, the gain medium was a [111]-cut Yb:YAG with a thickness of 0.5 mm and a doping concentration of 4 at. %. For the integrated chip-scale laser, the thickness was 0.35 mm and the doping concentration was 10 at. %. The saturable absorber was a 0.2 mm thick [100]-cut Cr:YAG with an initial transmittance of 95% for the mechanically assembled laser and 97% for the integrated chip-scale

laser. A short wave-pass filter ($R < 1\%$ at 940 nm, $R > 98\%$ at 1030 nm) and a long wave-pass filter ($R > 98\%$ at 940 nm, $R < 1\%$ at 1030 nm) were coated at one of the two surfaces of the Yb:YAG (the VECSEL side) and at the other surface of the Yb:YAG (the Cr:YAG side), respectively. An OC ($R = 85\%$ and 80% for the mechanically assembled and integrated chip-scale laser, respectively, at 1030 nm) was formed at the laser emitting surface of the Cr:YAG.

Device fabrication

To fabricate our laser, first, dielectric coating was formed on each surface of the GaAs substrate, the Yb:YAG, and the Cr:YAG using the conventional deposition method²². Second, each substrate was bonded one by one to the integrated structure using the wafer bonding technique, whose total thickness was 0.65 mm. After the bonding process, the integrated device was cut into 1 mm square chips by dicing. Finally, the fabricated laser chip was mounted onto a TO-can using Au–Sn solder paste and electrically connected through wire bonding.

Table 1 | Parameters used for simultaneous rate equations model

Symbol	Parameter	Value
η_i	Carrier injection efficiency	0.99
I_{off}	Offset current	0.49 A
G_0	Initial gain coefficient	$2.6 \times 10^5 \text{ s}^{-1}$
N_0	Carrier transparency number	1.8×10^5
β	Spontaneous emission coefficient	6.9×10^{-17}
ϵ	Gain compression coefficient	9.9×10^{-28}
k	Scale-factor of the output coupling efficiency	$1.0 \times 10^{-7} \text{ W}$
τ_n	Carrier lifetime in the VECSEL cavity	$9.9 \times 10^{-9} \text{ s}$
τ_p	Photon lifetime in the VECSEL cavity	$9.8 \times 10^{-12} \text{ s}$
I	Injected current	0.91 A
l_{sub}	Length of the GaAs substrate	0.1 mm
$t_V = 2(n_{sub}l_{sub} + n_{YAG}l_g)/c$	VECSEL external cavity round-trip time	$8.4 \times 10^{-12} \text{ s}$
A_{Yb}	Single-pass absorption rate of Yb:YAG	18.1%
σ_g	Stimulated emission cross section of Yb:YAG	$2.2 \times 10^{-20} \text{ cm}^2$
σ_{SA}	Ground-state absorption cross section of Cr:YAG	$4.6 \times 10^{-18} \text{ cm}^2$
σ_{ESA}	Excited-state absorption cross section of Cr:YAG	$8.2 \times 10^{-19} \text{ cm}^2$
l_g	Length of Yb:YAG	0.5 mm
l_{SA}	Length of Cr:YAG	0.2 mm
$N_{SAi} = -\ln(T_0^2)/(2\sigma_{SA}l_{SA})$	Total population density of Cr:YAG	$5.6 \times 10^{17} \text{ cm}^{-3}$
$t_r = 2n_{YAG}(l_g + l_{SA})/c$	Q-switched laser cavity round-trip time	$8.5 \times 10^{-12} \text{ s}$
τ_g	Lifetime of the upper laser level of Yb:YAG	$9.5 \times 10^{-4} \text{ s}$
τ_{SA}	Excited-state lifetime of Cr:YAG	$3.4 \times 10^{-6} \text{ s}$
γ_g	Inversion reduction factor of Yb:YAG	2
N_i	Total population density of Yb:YAG	$5.5 \times 10^{20} \text{ cm}^{-3}$
hc/λ_p	Photon energy	$2.1 \times 10^{-19} \text{ J}$
λ_p	Pumping wavelength	940 nm
F	Intensity adjustment factor	2.9
D	Diameter of pumping laser	0.16 mm
$V = \pi(D/2)^2 \times l_g$	Pumping volume	$1.0 \times 10^{-2} \text{ mm}^3$
L	Nonsaturable round-trip dissipative optical loss	0.05
c	Vacuum speed of light	$3.0 \times 10^8 \text{ m/s}$
q	Elementary charge	$1.6 \times 10^{-19} \text{ C}$
n_{sub}	Refractive index of the GaAs substrate	3.55
n_{YAG}	Refractive index of the laser crystal	1.82
R_{OC}	Reflectance of the OC	85%
T_0	Initial transmittance of Cr:YAG	95%

Pumping-power absorption model

With experimentally evaluated VECSEL output power (P_{exp}), the following equations are derived for the pumping-power absorption (P_{Yb}),

$$P_{cav}(R_{eff}) = P_{exp}(R_{eff}) \times \frac{T_{eff} + A_{eff}}{T_{eff}}, \tag{1}$$

$$P_{Yb} = P_{cav}(R_{eff1}) \times \frac{A_{eff1}}{T_{eff1} + A_{eff1}} \cdot \frac{A_{Yb}}{A_{Yb} + A_{GaAs}}, \tag{2}$$

where P_{cav} is the sum of the laser output power and absorbed power in the VECSEL cavity, which is referred to as the potential pumping power. An external cavity can be treated as one effective layer²³, and then, R_{eff} , T_{eff} , and A_{eff} are introduced as the effective reflectivity, effective transmissivity, and effective absorption rate of the external cavity part, respectively. They are calculated using Fabry-Perot resonance theory²⁴ under the maximum reflection condition (i.e., antiresonance condition) with parameters R_2 , R_{940} , and A_{GaAs} . P_{cav} is obtained for each R_{940} condition in the experiment (Fig. 2b) and is defined as a function of R_{eff} by interpolating the obtained data. As a next step, the pumping-power absorption P_{Yb} is derived. It is assumed that the same power of P_{cav} is obtained at the same effective reflectivity at steady state; therefore, P_{Yb} can be calculated by considering the absorbed portion by the Yb:YAG in the external cavity part when the effective parameters (R_{eff1} , T_{eff1} , and A_{eff1}) are changed according to the external cavity parameters (R_2 , R_3 , A_{GaAs} , and A_{Yb}). In addition to the major external cavity parameters, which are taken into account in this model, further consideration of other factors, such as diffraction and scattering losses, will contribute to realizing more accurate cavity design.

Simultaneous rate equations model

Table 1 summarizes the parameters used in the simultaneous rate equations model.

The carrier density N and photon density S in the VECSEL cavity of 940 nm are given by

$$\frac{dN}{dt} = \frac{\eta_i(I - I_{off})}{q} - \frac{N}{\tau_n} - \frac{G_0(N - N_0)S}{1 + \epsilon S}, \tag{3}$$

$$\frac{dS}{dt} = -\frac{S}{\tau_p} - \frac{2\alpha(S, N_g)}{t_V} + \frac{\beta N}{\tau_n} + \frac{G_0(N - N_0)S}{1 + \epsilon S}, \tag{4}$$

where $\alpha(S, N_g) = A_{Yb} \times S \times (1 - N_g/N_i)$ is the absorbed photon density in the Yb:YAG, which indicates the loss of the VECSEL cavity. Equations (3) and (4) are the modified semiconductor laser rate equations of the VECSEL cavity based on the equations of VCSEL²⁵. The parameters listed in Table 1 from η_i to τ_p were extracted from I-L and current-voltage profiles under the maximum output condition shown in Fig. 2b.

The photon density (ϕ), population inversion density of the Yb:YAG (N_g), and ground-state population density of the Cr:YAG (N_{SA}) in the passively Q-switched laser cavity of 1030 nm are respectively given by

$$\frac{d\phi}{dt} = \frac{\phi}{t_r} [2\sigma_g N_g l_g - 2\sigma_{SA} N_{SA} l_{SA} - 2\sigma_{ESA} (N_{SAi} - N_{SA}) l_{SA} - (L - \ln R_{OC})], \tag{5}$$

$$\frac{dN_g}{dt} = W(\alpha(S, N_g)) - \frac{N_g}{\tau_g} - \gamma_g \sigma_g c \phi N_g, \tag{6}$$

$$\frac{dN_{SA}}{dt} = \frac{N_{SAi} - N_{SA}}{\tau_{SA}} - \sigma_{SA} c \phi N_{SA}, \tag{7}$$

where $W(\alpha(S, N_g)) = \alpha(S, N_g) \times k \times F / (hc/\lambda_p \times V)$ is the volume pumping rate into the upper laser level, which indicates the pumping intensity of the Yb:YAG. Equations (5)–(7) are the modified rate equations of the passively Q-switched laser cavity based on equations of solid-state lasers^{26,27}. The rate equations of the semiconductor and the solid-state lasers can be coupled by the existence of a common $\alpha(S, N_g)$. Therefore, the oscillation mechanism of the proposed laser can be simulated by solving the Eqs.

(3)–(7) numerically. Note that to provide a qualitative description of the behavior of the laser cavities, our model simplifies some conditions of the actual laser configuration. A quantitative analysis will be discussed in future studies.

Reporting summary

Further information on experimental design is available in the Nature Research Reporting Summary linked to this paper.

Data availability

The authors declare that the source data generated in this study are provided with this paper.

References

- Ding, K. et al. Aerosol-boundary-layer-monsoon interactions amplify semi-direct effect of biomass smoke on low cloud formation in Southeast Asia. *Nat. Commun.* **12**, 6416 (2021).
- Cézard, N. et al. Performance assessment of a coherent DIAL-Doppler fiber lidar at 1645 nm for remote sensing of methane and wind. *Opt. Express* **28**, 22345–22357 (2020).
- Gattass, R. R. & Mazur, E. Femtosecond laser micromachining in transparent materials. *Nat. Photon.* **2**, 219–225 (2008).
- Phillips, K. C. et al. Ultrafast laser processing of materials: a review. *Adv. Opt. Photon.* **7**, 684–712 (2015).
- Abbasi, H. et al. Highly flexible fiber delivery of a high peak-power nanosecond Nd:YAG laser beam for flexiscopic applications. *Biomed. Opt. Express* **12**, 444–461 (2021).
- Cosgrove, R. J. et al. Disruption of ingrown epithelium via Nd:YAG laser or DIEYAG. A retrospective case series of Post-LASIK patients. *Am. J. Ophthalmol. Case Rep.* **22**, 101701 (2021).
- Zervas, M. N. & Codemard, C. A. High power fiber lasers: a review. *IEEE J. Sel. Top. Quantum Electron.* **20**, 219–241 (2014).
- Giesen, A. & Speiser, J. Fifteen years of work on thin-disk lasers: results and scaling law. *IEEE J. Sel. Top. Quantum Electron.* **13**, 598–609 (2007).
- Schmidt, B. E. et al. Highly stable, 54 mJ Yb-Innoslab laser platform at 0.5 kW average power. *Opt. Express* **25**, 17549–17555 (2017).
- Zayhowski, J. J. & Mooradian, A. Single-frequency microchip Nd lasers. *Opt. Lett.* **14**, 24–26 (1989).
- Lim, H. H. & Taira, T. >50 MW peak-power, high brightness Nd:YAG/Cr⁴⁺:YAG microchip laser with unstable resonator. *Opt. Express* **30**, 5151–5158 (2022).
- Maiman, T. H. Stimulated optical radiation in ruby. *Nature* **187**, 493–494 (1960).
- Huber, G. et al. Solid-state lasers: status and future. *J. Opt. Soc. Am. B* **27**, 93–105 (2010).
- Koehnner, W. *Solid-State Laser Engineering. Sixth Revised and Updated Edition.* (Springer, VA, 2006).
- Patel, F. D. et al. Laser demonstration of Yb₃Al₅O₁₂ (YbAG) and materials properties of highly doped Yb:YAG. *IEEE J. Quantum Electron.* **37**, 135–144 (2001).
- Giudice, G. E. et al. Differential carrier lifetime in oxide-confined vertical cavity lasers obtained from electrical impedance measurements. *Appl. Phys. Lett.* **74**, 899 (1999).
- Kusters, A. M. et al. Carrier lifetime measurement in semiconductor lasers using injection current pulses of Gaussian shape. *IEEE J. Quantum Electron.* **28**, 2669–2673 (1992).
- Morita, R. et al. Photonic-crystal lasers with two-dimensionally arranged gain and loss sections for high-peak-power short-pulse operation. *Nat. Photon.* **15**, 311–318 (2021).
- Yu, N. & Capasso, F. Flat optics with designer metasurfaces. *Nat. Mater.* **13**, 139–150 (2014).
- Ancona, A. et al. Femtosecond and picosecond laser drilling of metals at high repetition rates and average powers. *Opt. Lett.* **34**, 3304 (2009).
- Hofmann, O. et al. Design of multi-beam optics for high throughput parallel processing. *J. Laser Appl.* **32**, 012005 (2020).
- Macleod, H. A. *Thin-Film Optical Filters 3rd edition.* (CRC Press, NY, 2000).
- Coldren, L. A. et al. *Diode Lasers and Photonic Integrated Circuits 2nd edition.* (Wiley, NJ, 2012).
- Yariv, A. & Yeh, P. *Photonics 6th edition.* (Oxford University Press, Oxford, 2007).
- Yuan, Z. et al. Modeling, extraction and verification of VCSEL model for optical IBIS AML. *Proc. DesignCon.* (2014).
- Dong, J. Numerical modeling of CW-pumped repetitively passively Q-switched Yb:YAG lasers with Cr:YAG as saturable absorber. *Opt. Commun.* **226**, 337–344 (2003).
- Ma, J. et al. Optimization of Yb:YAG/Cr⁴⁺:YAG composite ceramics passively Q-switched microchip lasers. *Appl. Phys. B* **105**, 749–760 (2011).

Acknowledgements

We acknowledge technical support for VCSEL fabrication from Yuta Yoshida, Masato Oishi, Yuta Otoguro, and Naoto Kikuchi at Sony Semiconductor Manufacturing Corporation, for dielectric coating from Yasuro Nakagawa and Shohei Abe at Sony Global Manufacturing and Operations Corporation.

Author contributions

All authors contributed extensively to the work presented in this paper. M.K. conceived the original concept. M.K., G.H., J.Y., K.T., R.K., and Y.H. designed the basic chip-scale laser structure. G.H. and H.W. designed the VCSEL devices. G.H. fabricated and tested the VCSEL devices. M.S., G.Y., H.T., and Y.I. fabricated the chip-scale laser and performed the measurements. K.T. and J.Y. performed the theoretical analysis and the rate equation simulation. J.Y., K.T., G.H., G.Y., and M.K. wrote the paper. M.K. supervised the project with K.Y.

Competing interests

M.K., G.Y., G.H., and K.T. are inventors in several patent applications related to this work filed by Sony Group Corporation (including PCT patent application no. PCT/JP2020/043292). The authors declare that they have no other competing interests.

Additional information

Supplementary information The online version contains supplementary material available at <https://doi.org/10.1038/s41467-022-33528-x>.

Correspondence and requests for materials should be addressed to Masanao Kamata.

Peer review information *Nature Communications* thanks Alexander Fuerbach, Masayuki Suzuki and the other anonymous reviewer(s) for their contribution to the peer review of this work. Peer review reports are available.

Reprints and permission information is available at <http://www.nature.com/reprints>

Publisher's note Springer Nature remains neutral with regard to jurisdictional claims in published maps and institutional affiliations.

Open Access This article is licensed under a Creative Commons Attribution 4.0 International License, which permits use, sharing, adaptation, distribution and reproduction in any medium or format, as long as you give appropriate credit to the original author(s) and the source, provide a link to the Creative Commons license, and indicate if changes were made. The images or other third party material in this article are included in the article's Creative Commons license, unless indicated otherwise in a credit line to the material. If material is not included in the article's Creative Commons license and your intended use is not permitted by statutory regulation or exceeds the permitted use, you will need to obtain permission directly from the copyright holder. To view a copy of this license, visit <http://creativecommons.org/licenses/by/4.0/>.

© The Author(s) 2022